Optimized Surface H Absorption by Atomically S Filling in Oxygen Vacancies Boosts Hydrogen Evolution Reaction

Jing Jin,[a] Jie Yin,[a] Hongbo Liu,[b] Bolong Huang,*,[c] Yang Hu,[a] Min Lu,[a] Hong Zhang,[d] Nan Zhang,[a] Jianyi Li,[a] Rui Yang,[a] Mingzi Sun,[c] Yong Peng,[d] Pinxian Xi,*,[a] and Chun-Hua Yan[a],[e]

Dedication ((optional))

Abstract: Hydrogen evolution reaction (HER) normally has sluggish kinetics in alkaline solutions due to the difficulty of forming binding protons. Herein we report a novel electrocatalyst by sulfur atoms doping into hybrid spinel $NiFe_2O_4$, which is conducive to generate H_{ads} in alkaline conditions for the Volmer step. This novel electrocatalyst has an ultralow overpotential of 61 mV at the current density of 10 mA cm^{-2} in 1 M KOH media and long-term stability under the large current density, which are much superior to the state-of-the-art Ni-Fe based catalysts. *In-situ* Raman spectroscopy revealed that the adsorptions of the sulfur atom with high electron density, coupling with oxygen vacancies, is more likely to *in-situ* form S-H_{ads} for boosting HER in the alkaline solution. DFT calculations further verified lowered energy barrier of the H_2O dissociation induced by the S introduction is the key reason for the remarkable HER performance. This work will open up a new insight into designing non-metal atom doped electrocatalysts to accelerate water splitting and enhance the efficiency of alkaline HER

[a] J. Jin, J. Yin,Y.Hu, M. Lu, N. Zhang, J. Li, R. Yang, Prof. P. Xi and Prof. C.-H. Yan
State Key Laboratory of Applied Organic Chemistry, Key Laboratory of Nonferrous Metal Chemistry and Resources Utilization of Gansu Province, College of Chemistry and Chemical Engineering, Lanzhou University, Lanzhou 730000, China.
E-mail: xipx@lzu.edu.cn
[b] H. Liu
Lanpec Technologies Limited, Shanghai 200000, China.
[c] M. Sun, Prof. B. Huang
Department of Applied Biology and Chemical Technology, The Hong Kong Polytechnic University, Hong Hum, Kowloon, Hong Kong SAR, China.
[d] H. Zhang, Prof. Y. Peng
Key Laboratory of Magnetism and Magnetic Materials of Ministry of Education, School of Physical Science and Technology, Lanzhou University, Lanzhou 730000, China.
[e] Prof. C.-H. Yan
Beijing National Laboratory for Molecular Sciences, State Key Laboratory of Rare Earth Materials Chemistry and Applications, PKU-HKU Joint Laboratory in Rare Earth Materials and Bioinorganic Chemistry, Peking University, Beijing 100871, China.
[#] These authors contributed equally to this work.

Introduction

Electrocatalyst water splitting will hopefully become one of the mainstream hydrogen production technologies in the future.[1-2] There are three main technical routes for hydrogen generation: the alkaline hydrolysis cell (AE), the proton exchange membrane water electrolysis cell (PEM) and the solid oxide water electrolysis cell (SOE). Compared with PEM, AE is an economical approach because of the replacement of expensive proton exchange membranes, the improved long-term stability, and massive H_2 production system. However, the sluggish kinetics and high-power consumption of the alkaline HER are emerging as the main obstacles to realize the better H_2 economy.[3-9] To date, Pt-based compounds are the most effective catalysts for HER in alkaline solution, but the high price, increasing scarcity, and poor stability of noble metal heavily hinder them from widespread applications.[10-16] Thus, an innovatory strategy on designing efficient, low-cost and stable non-noble metal catalysts for alkaline HER is highly desired.

For alkaline HER, the rate-limiting step is the Volmer step ($H_2O+e^- \rightarrow H_{ads}+OH^-$).The unsatisfactory production rate of H_{ads} has an adverse impact on the water dissociation process.[17-19] Therefore, a comprehensive investigation on the HER mechanism in alkaline solution through the in-situ characterization of (E refers to the active site) the intermediate formation process for E-H_{ads} becomes more and more important.[20] Furthermore, an effective catalyst, which can form the intermediate at relatively low overpotential under the alkaline condition, will perform the high electrocatalytic activity and largely increase the efficiency of alkaline HER.[21-24] Accordingly, it is essential to design a new-type non-noble catalyst for overcoming the intrinsic weakness of traditional catalysts, such as sluggish catalytic kinetics and poor stability, to further promote the reaction kinetics and improve the catalytic activity.

Herein, we contribute a new metal oxide catalyst (S-$NiFe_2O_4$) by doping sulfide into hybrid spinel $NiFe_2O_4$ to change the chemical environment of Fe metal sites and couple the electronegative S sites with oxygen vacancies. This kind of new structure can boost the formation of S- H_{ads}•H_2O intermediate and accelerate the reaction process, which leads to the excellent catalytic activity for HER in alkaline solution. DFT calculations indicated that the introduction of S causes the local structural distortion of tetrahedral Fe to octahedral sites, and the H_2O adsorption energy shows a downhill trend, which lays a good initiation of HER. Thus, this is the

This is the peer reviewed version of the following article: J. Jin, J. Yin, H. Liu, B. Huang, Y. Hu, H. Zhang, M. Sun, Y. Peng, P. Xi, C.-H. Yan, Atomic Sulfur Filling Oxygen Vacancies Optimizes H Absorption and Boosts the Hydrogen Evolution Reaction in Alkaline Media, Angew. Chem. Int. Ed. 2021, 60, 14117., which has been published in final form at https://doi.org/10.1002/anie.202104055.

essential key for S-$NiFe_2O_4$ to enhance intrinsic catalytic activity and promote the catalytic performance of HER. In strong alkaline electrolytes (for example, 1.0 M KOH), the S-$NiFe_2O_4$ catalyst shows an overpotential of only 61 mV at a current density of 10 mA cm^{-2}, which are superior to the recently reported breakthrough HER catalysts.[25,26] According to the results, we conclude that the tailored control on the electronic structure of oxides will open significant opportunities for the rational design of electrocatalysts from earth-abundant and stable materials.

Results and Discussion

The S-$NiFe_2O_4$ nanoparticles were synthesized by a low temperature vulcanization method, which put $NiFe_2O_4$ precursor under sulfur steam at 180°C for 2h and doped S atoms into $NiFe_2O_4$ precursor, the illustration of the synthesis route is shown in Figure 1a. According to the X-ray powder diffraction (XRD) patterns in Figure 1b, the S-$NiFe_2O_4$ nanocrystal displays the same crystal structure as the cubic $NiFe_2O_4$ with a space group of Fd3m (JCPDS No. 10-325, a = b = c = 8.339 Å). Obviously, there are no structural changes compared with $NiFe_2O_4$ precursor after S doping, indicating that the low temperature vulcanization method did not introduce new phases inside the $NiFe_2O_4$ precursor. Transmission electron microscopy (TEM) was employed to characterize the morphology of S-$NiFe_2O_4$ nanocrystal, which showed that the S-$NiFe_2O_4$ appeared as nanoparticles with an average size of 10 nm (Figure S1 and S2) with the same structure with $NiFe_2O_4$ precursor (Figure S3). Although XRD pattern and morphology has no changes after S doping, it is necessary to further prove the successful incorporation of S atoms into $NiFe_2O_4$. The atomic resolution HADDF-STEM image revealed that the fine structure of S-$NiFe_2O_4$ can be identified as a heterostructure constructed by basic $NiFe_2O_4$ spinel structure with [-112] orientation and additional FeS_2 hcp structure with [011] orientation (Figure 1c), indicating that the S doping in $NiFe_2O_4$ has involved Fe-S in local areas, as shown in Figure 1a. FFT-filtered atomic resolution image was further used to visualize the domain transformation (Figure 1d). And the corresponding line intensity profiles in Figure S4 can directly display the different periodic atom arrangements of A and B area, which confirm the doping of S results in lattice distortion, the bonding form of metal cations has been changed. The EDS elemental mapping images of the selected area show the uniform distributions of doped S, Ni, Fe and O on the district can also prove the incorporation of S atoms (Figure S5) and the contents of S, Ni, Fe and O can be measured by EDS spectra (Figure S6). Apart from that, S doping also made S-$NiFe_2O_4$ accompanied surface reconstruction from (001) to (311), which was reflected by the HRTEM of the catalysts (Figure S7 and S8). In addition, The Fast Fourier transform (FFT) images in Figure 1e show the coexistence of two clearly distinct structural domains. And from Figure 1f-h, more atomic-resolution HAADF-STEM images and EDS atomic elemental mappings further prove $NiFe_2O_4$ is an ideal inverse spinel structure. Thus, all the above results verified the successful production of S-$NiFe_2O_4$ which changing the coordination environment of part of Fe cations.

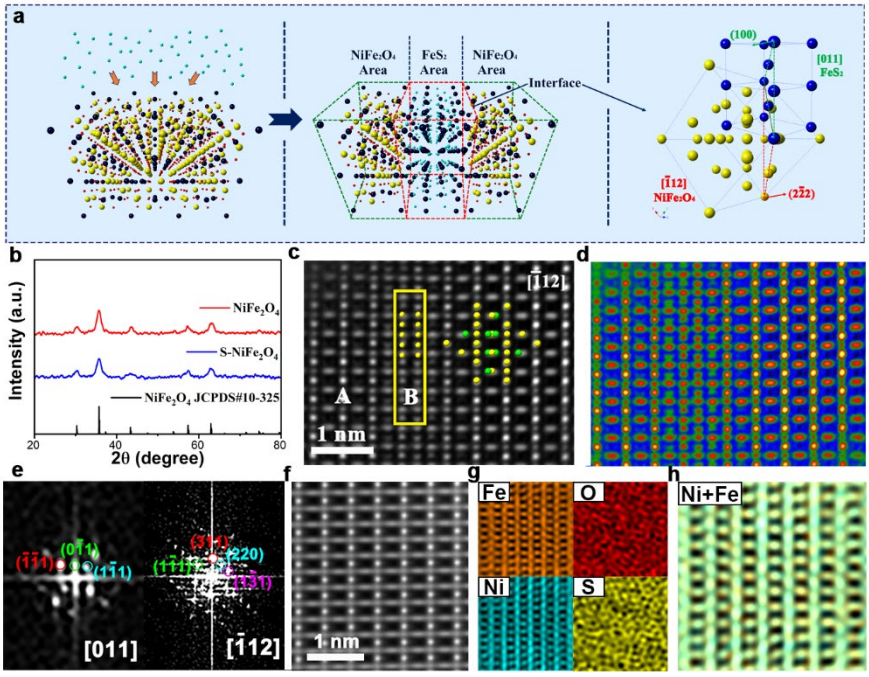

Figure 1. a) Schematic illustration of the synthesis of S-$NiFe_2O_4$ b) XRD patterns of $NiFe_2O_4$ and S-$NiFe_2O_4$, c) c) HAADF-STEM image of S-$NiFe_2O_4$. The insets show the corresponding crystal structure of S-$NiFe_2O_4$ unit cells taken along the [−112] orientation and the corresponding FFT patterns for the HAADF-STEM image of S-$NiFe_2O_4$; d) FFT-filtered atomic resolution image using two sets of diffraction spots e) the corresponding FFT patterns for the HAADF-STEM image of

A and B domains; Perspective view of unit cells along [−112] orientations; f) Atomic-resolution HADDF-STEM image viewed from the [−112] orientation. g,h) EDX atomic-scale mappings of Ni, Fe, O, S elements.

The chemical and electronic states of S-$NiFe_2O_4$ nanocrystal were further confirmed by a series of structural characterizations. Electron Spin Resonance (ESR) spectra was usually used to illustrate the variation of V_o. [24,27-28] As shown in Figure 2a, the ESR signal of S-$NiFe_2O_4$ is slightly weaker than $NiFe_2O_4$, which results from S atoms doping into $NiFe_2O_4$ and coupling with oxygen vacancies. And from Figure 2b, the X-ray photoelectron spectroscopy (XPS) of O1s can be divided into three peaks,[29-31] lattice oxygen (O-M) at 529.8 eV, coordinatively unsaturated oxygen or oxygen in hydroxyl group (OOH) at 531.4 eV, and oxygen in adsorbed water (O_{H2O}) at 532.5 eV. Compared with the $NiFe_2O_4$ precursor, the banding energy of O 1s XPS spectra of S-$NiFe_2O_4$ display a positive shift about 0.3 eV, which indicates a higher surface coupling after S doping into $NiFe_2O_4$. Additionally, The X−ray absorption near−edge structure (XANES) spectra of O K−edge (Figure S9) further proved that the O 1s core level to the unoccupied O 2p states hybridized with M 3d orbitals, suggesting that S-$NiFe_2O_4$ has stronger metal-oxygen covalency. Meanwhile, the UPS spectra in Figure 2c illustrated S atoms doping, S-$NiFe_2O_4$ has slightly shifted with $NiFe_2O_4$. Hence, the successful incorporation of S atoms to the $NiFe_2O_4$ structure has changed the chemical environment of metal sites in the $NiFe_2O_4$.

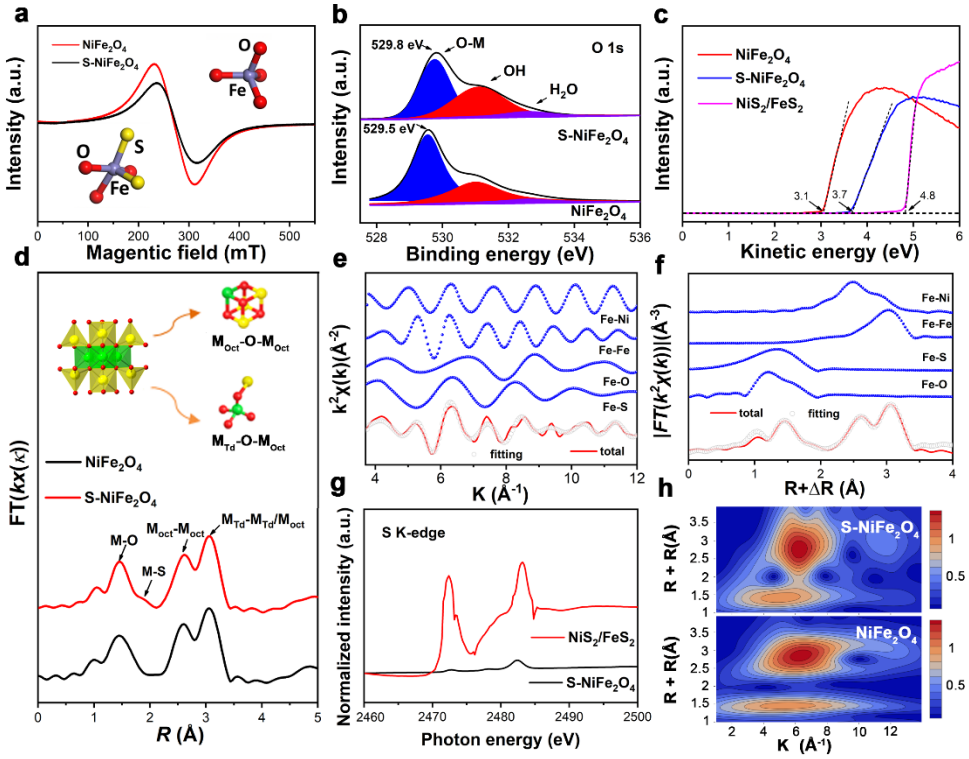

Figure 2. Structural characterization a) ESR spectra of $NiFe_2O_4$ and S-$NiFe_2O_4$, b) O 1s spectra of $NiFe_2O_4$ and S-$NiFe_2O_4$, c) UPS spectra of $NiFe_2O_4$ and S-$NiFe_2O_4$, d) EXAFS spectra of $NiFe_2O_4$ and S-$NiFe_2O_4$ at Fe K-edge. e,f) EXAFS k3 (R) spectra data (lines) and fitting curves (grey dots) of S-$NiFe_2O_4$ in k (e) and R (f) spaces at Fe K-edge and curves about four kinds of binding patterns of Fe (blue dots). g) the illustration of surface reconstruction, h) the corresponding wavelet transforms for the k3−weighted Fe K−edge EXAFS signals of S-$NiFe_2O_4$ and $NiFe_2O_4$.

As awell-known material, $NiFe_2O_4$ is an ideal inverse spinel structure, in which Ni^{2+} normally occupied the octahedral sites and Fe^{3+} occupied the octahedral and tetrahedron sites, respectively. Though the extended X-ray absorption fine structure spectroscopy (EXAFS) spectra (Figure 2d), in cubic spinel structure has two kinds of atomic distances which contain with M_{Td}-M_{Td}/M_{Oct} and MO_{ct}-M_{Oct}. The atomic distance of M_{Td}-M_{Td}/M_{Oct} are ~3.0 Å, represent between the two nearest tetrahedral cations and between the tetrahedral cation to the nearest octahedral cation respectively, and the atomic distance of M_{Oct}-M_{Oct} are ~2.5 Å was between the two octahedral cations. [33] As shown in the insert picture of Figure 2d, though a simple model, represents two bonding modes about octahedral and tetrahedron sites. The fact that Fe atoms exist at both octahedral sites and tetrahedral sites and formed Fe-S in the S-$NiFe_2O_4$ structure. S 2p XPS spectra of S-$NiFe_2O_4$ also proved formed Fe-S structure (Figure S10). The fitting results of the Fe K-edge EXAFS spectrum (Figure S11, Table S2) showed

that the coordination number of Fe has enhanced in the S-$NiFe_2O_4$, indicating some Fe cations corporation with S atom. From Figure 2e and f, the coordination configuration in S-$NiFe_2O_4$ nanocrystal was further investigated by quantitative least-squares EXAFS curve-fitting analysis and S atoms has been filled with trace form, the S-$NiFe_2O_4$ compared with NiS_2/FeS_2 which has been completely vulcanization performs weakly signal in S K-edge XANES spectra, and S-$NiFe_2O_4$ exhibits a distinct negative shift about 0.9 eV compared with NiS_2/FeS_2, originating from smaller transition energy (S 1s→S 3p), which generate a high electroactivity surface in the crystal structure (Figure 2g), simultaneously, this surface S sites normally have high sensitivity for adsorbing H_2O. The S-$NiFe_2O_4$ structure was further demonstrated by the wavelet transform (WT) of Fe K-edge EXAFS as shown in Figure 2h. In line with the FTs, the WT analysis of S-$NiFe_2O_4$ and $NiFe_2O_4$ spinel structure have similar coordination intensities at ~6.3 $Å^{-1}$, indicating the same spinel structure. Apart from that, the successful incorporation of S atoms into the $NiFe_2O_4$ structure has changed chemical environment of different elements in the $NiFe_2O_4$. Combined with the X-ray photoelectron spectroscopy (XPS) of Fe 2p (Figure S14), S-$NiFe_2O_4$ moved towards to higher field of 0.32 eV than $NiFe_2O_4$, indicating S atoms doped into $NiFe_2O_4$ has enhanced the coordination ability of Fe. Additionally, the calculated results show the relative intensity of Fe^{3+}/Fe^{2+} for S-$NiFe_2O_4$ (1.69:1), which is lower than that of $NiFe_2O_4$ (1.82:1) (Table S2), suggesting the formation of FeS_2 structure and these Fe cations from tetrahedron occupied transform into octahedral occupied.

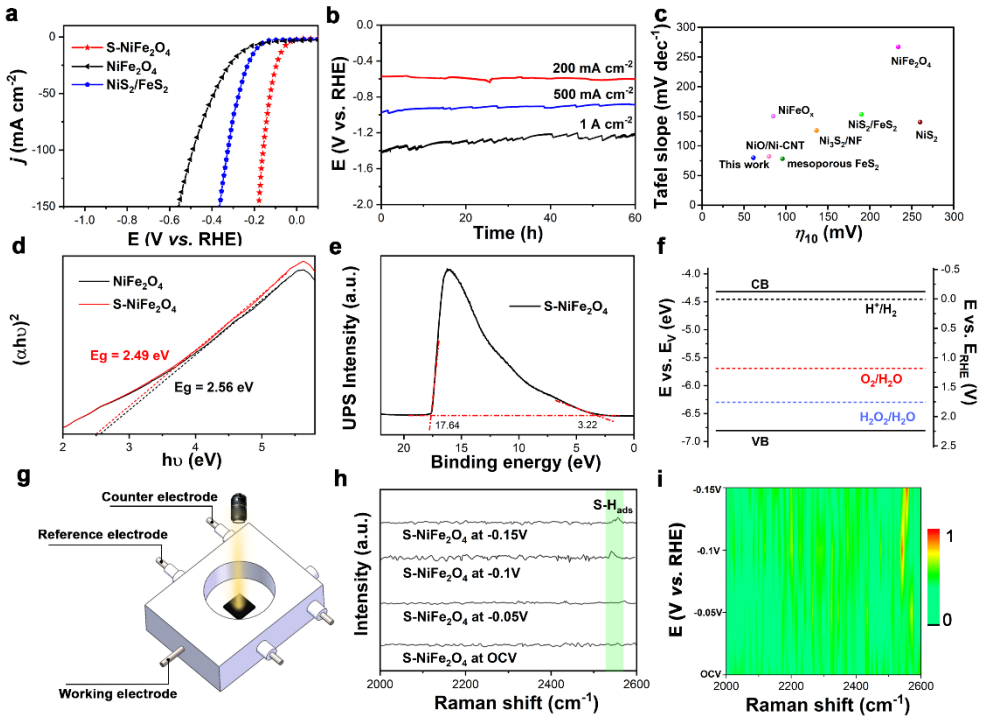

Figure 3. a) IR-corrected LSV curves of $NiFe_2O_4$, NiS_2/FeS_2 and S-$NiFe_2O_4$ for HER in 1.0 M KOH, b) Chronoamperometric response of the S-$NiFe_2O_4$ at different current densities for HER, c) Comparison of merit with respect to both kinetics (Tafel slope) and activity, d) $(αhv)^2$ versus hv curve of $NiFe_2O_4$ (black curve) and S-$NiFe_2O_4$ (red curve). The intersection value is the bandgap, e) UPS spectra of S-$NiFe_2O_4$ (black curve). The dashed red lines mark the baseline and the tangents of the curve. The intersections of the tangents with the baseline give the edges of the UPS spectra from which the UPS width is determined, f) Band structure diagram for S-$NiFe_2O_4$, g) Schemes of in-situ Raman spectrometry, h) and i) In situ Raman signals of S-$NiFe_2O_4$ during HER.

The HER catalytic activity of those materials was applied as the working electrode and evaluated by linear scan voltammogram (LSV) in N_2-saturated 1.0 M KOH electrolyte (pH = 14). As seen, S-$NiFe_2O_4$ nanocrystal shows excellent HER performance (Figure 3a) with the overpotential of only 61 mV at the current density at 10 mA cm^{-2}, which is much better than those contrast materials including$NiFe_2O_4$ (234 mV) and NiS_2/FeS_2 (190 mV). Additionally, the Tafel plots (log j~□) also play a significant role in electrocatalytic, which can be further measured to confirm the HER rate of those catalysts, S-$NiFe_2O_4$ has the smallest Tafel role (80 mV dec^{-1}) than other contrast materials, indicating the faster HER kinetics on S-$NiFe_2O_4$ (Figure S13). Besides, stability is one of the important criteria to measure the performance of the catalyst. From Figure 3b, S-$NiFe_2O_4$ nanocrystal performs perfect stability at different large current densities (200, 500 and 1000mA cm^{-2}) for 60 h in alkaline media with a negligible overpotential change. Electrochemical impedance spectroscopy (EIS) analysis (Figure S14) shows electronic conductivity of S-$NiFe_2O_4$ is enhanced with

low solution resistance (Rs) of 1.42 Ohm and charge-transfer resistance (Rct) of 2.27 Ohm (Table S3). Among some representative HER catalysts reported, the S-$NiFe_2O_4$ with present state-of-the-art alkaline HER catalysts (Fig. 3c and Table S4). [34-36]

This catalyst performs excellent catalytic activity because of an appropriate band alignment andwe used ultraviolet photo-electron spectroscopy (UPS) and ultraviolet-visible (UV-vis) absorption to determine the E_g and E_v of these catalysts. As shown in Figure 3d, calculated from UV-vis, the bandgap values are 2.49 eV and 2.56 eV for S-$NiFe_2O_4$ and $NiFe_2O_4$, respectively. The slight differences between S-$NiFe_2O_4$ and $NiFe_2O_4$ is mainly due to only small amount of S atom have been introduced And from Figure 3e, the ionization potential [equivalent to the valence band energy (E_v)] was calculated to be 6.80 eV by subtracting the width of the He I UPS spectra from the excitation energy (21.22 eV) and the conduction band energy E_c is thus estimated at 4.31 eV from E_v– E_g.[37] From Figure 3f, these bands are properly positioned to accelerate theelectron transfer, making S-$NiFe_2O_4$ a promising catalyst for HER.

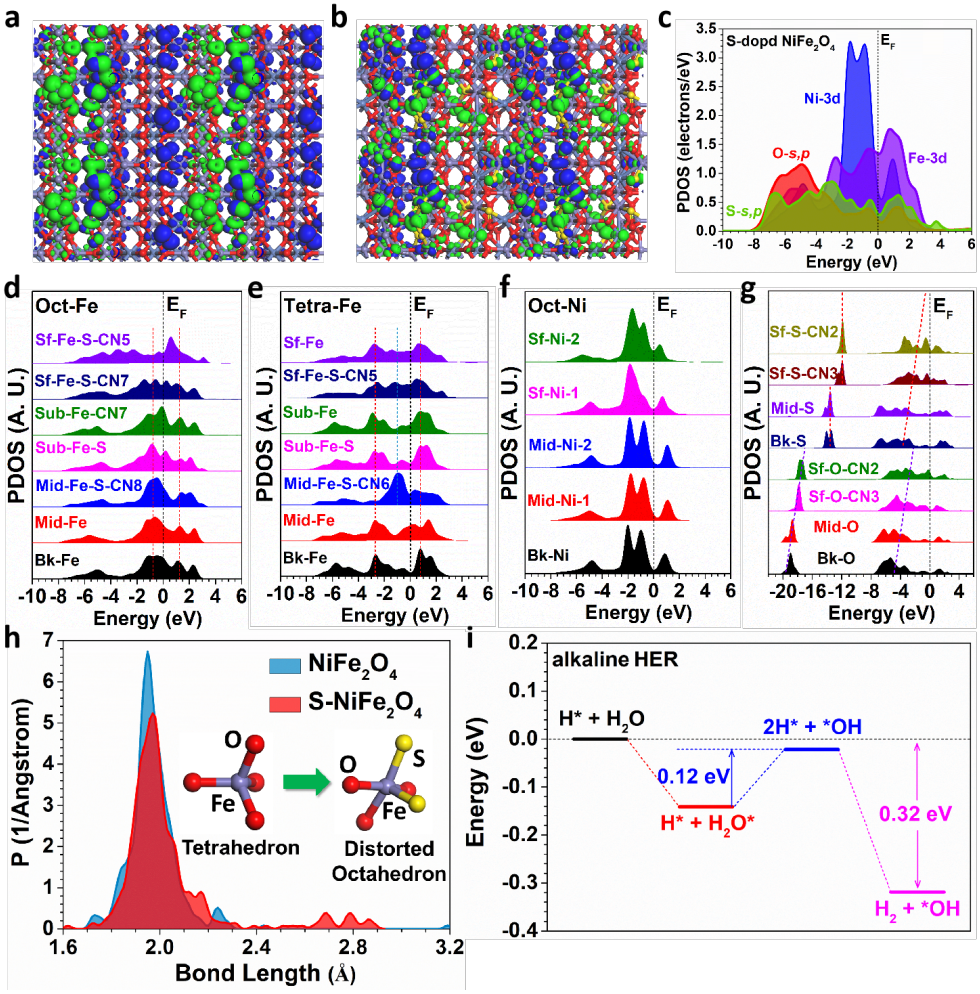

Figure 4. (a) The bonding and anti-bonding orbitals near E_F of (a) $NiFe_2O_4$ and (b) S-$NiFe_2O_4$. (c) The PDOS of S-$NiFe_2O_4$. (d) The site-dependent PDOSs of octahedral Fe sites. (e) The site-dependent PDOSs of tetrahedral Fe sites. (f) The site-dependent PDOSs of octahedral Ni sites. (g) The site-dependent PDOSs of S and O sites. (h) The bond length distribution of $NiFe_2O_4$ and S-$NiFe_2O_4$. Insets are the display of the structural change from tetrahedral Fe sites in NiFe2O4 to distorted tetrahedral Fe sites in S-$NiFe_2O_4$. (i) The energetic reaction trend of S-$NiFe_2O_4$ electrocatalyst for HER in the alkaline environment.

Apart from that, to further explore the mechanism of HER, in-situ Raman spectroscopy as shown in Figure 3g was used to study the reaction intermediates. from Figure 3h and Figure 3i, with the potential gradually going down, a peak at ~ 2530 cm^{-1} was

observed when the potential reaches -0.1V and -0.15 V (vs RHE). This band is ascribed to the stretching vibration of S-H_{ads} and formed this S-H_{ads} intermediate on the S-$NiFe_2O_4$ during the HER can promote the catalytic reaction. Therefore, the surface S atoms with high electron density are more conducive to absorbing H_{ads} intermediate which are confirmed to be the active sites for HER.

The improver HER performance of S-$NiFe_2O_4$ has also been investigated by DFT calculations. Based on the experimental characterizations, all the Ni has been located in the octahedral sites while Fe atoms occupy half octahedral and half tetrahedral sites, respectively. Meanwhile, the introduced S sites are mainly located near Fe sites with the formation of Fe-S bonds, which causes the local distortion near Fe sites without inducing the evident change on the morphologies of the crystal structures, which is consistent with the experiments. Meanwhile, from the bonding and anti-bonding orbital distribution near the Fermi level (E_F), the pristine $NiFe_2O_4$ displays the electron-rich structures near the surface O sites and the octahedron Fe sites. The local distortion of the lattice also results in the perturbation of the electronic distribution, in which the electroactivity of the surface metal sites has been activated (Figure 4a-4b). The projected partial density of states (PDOSs) indicates the electronic structures of different elements in S-$NiFe_2O_4$. We notice the slight barrier between the t_{2g} and e_g of Fe-3d orbitals, supporting a high electroactivity. The close position of Ni sites near EF also facilitates the stable H adsorption during the alkaline HER process. Both s,p orbitals of O and S cover a broad range from E_V-8.0 eV towards E_V+4.0 eV (E_V = 0 eV), which play as the electron suppliers for the Fe-sites to activate the H_2O molecules (Figure 4c). Since the S introduction leads to the local distortion of the lattice, the site-dependent PDOSs are important to unravel the chemical environment of different elements for HER. For the octahedral Fe sites, the 3d bands only show very limited change from the bulk towards the surface, which demonstrates a stable electroactivity for the HER process (Figure 4d). In contrast, the Fe in tetrahedral sites exhibits a sensitivity to the coordination environment. Meanwhile, as the increases of Fe coordination number to 6 as the octahedron environment, the Fe-3d bands also display a similar PDOSs to the octahedral Fe sites, supporting the improvement of the electronic structures induced by the local crystal structure, which are consistent with the experiments (Figure 4e). The Ni sites have preserved the high electroactivity in the crystal structures, which has been affected by the introduction of S atoms. The stable electroactivity of Ni sites guarantees the efficient H adsorption during HER (Figure 4f). In addition, the electronic structures of O and S are compared. From the bulk structure to the surface, both O and S show the gradual upshifting of the s,p orbitals, in which the S-s,p orbitals support a closer position to the E_F to achieve a smaller electron transfer barrier from S-sites to Fe-sites. Such an electronic environment guarantees efficient HER (Figure 4g).

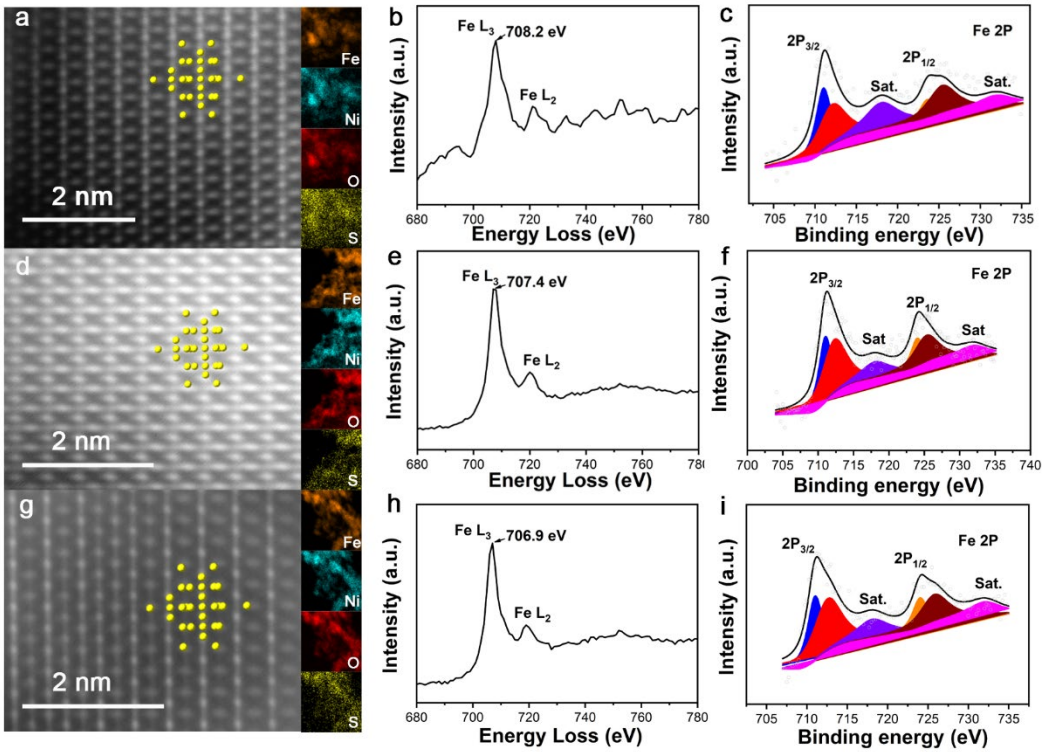

Figure 5. (a, d, g) Atomic-resolution HADDF-STEM image for S-$NiFe_2O_4$ at OCV, -1V and -1.2V, respectively. (b, e, h) Fe–L edge EELS profiles for S-$NiFe_2O_4$ at OCV, -1V and -1.2V, respectively. (c, f, i) Fe 2p XPS spectra for S-$NiFe_2O_4$ at OCV, -1V and -1.2V, respectively.

To further look into the structural change induced by the S introduction, we also monitor the bond length distribution in both $NiFe_2O_4$ and S-$NiFe_2O_4$. For the pristine $NiFe_2O_4$, the bond length is dominantly distributed near 1.95 Å, which are attributed by both the octahedral and tetrahedral sites with well-ordered structures. However, the introduction of S enlarges the main bond length distribution to 1.97 Å, supporting the local distortion. Meanwhile, we also notice the enhanced concentration of larger bond length, which is ascribed to the change from tetrahedron to the octahedron. In the S-$NiFe_2O_4$, we have noticed the tetrahedral sites of Fe has changed into the distorted octahedral sites, where the coordination number also increases from 4 to 6. These results have further verified the structure change induced by S introduction in experiments (Figure 4h). In the end, the reaction energy trend of HER in the alkaline has been illustrated. The initial H_2O adsorption shows the spontaneous reaction with -0.14 eV energy downhill trend, which lays a good initiation of HER. Then the rate determining step of H_2O dissociation demonstrates a smaller barrier height of 0.12 eV. The subsequent formation of H_2 is strongly exothermic with 0.30 eV energy release. The total process of HER in the alkaline demonstrates overall energy of -0.32 eV, supporting the energetically preferred process without overbinding of formed H_2 to lower the HER efficiency (Figure 4i).

After the HER catalytic test, we observed the chemical environment of S-$NiFe_2O_4$ nanocrystal. According to the Atomic-resolution HADDF-STEM images, this catalyst still maintains the original crystal structure under different test potentials, OCV, -1V and -1.2V, respectively. And the corresponding elemental mappings have shown that the homogeneous distribution of Ni, Fe, O and S throughout the nanocrystal (Figure 5a,5d and 5g). Furthermore, the EELS spectrum indicated that the valence state of Fe decreased (Figure 5b,5e and 5h) after HER, which may attribute to the reduction of surface metal during HER process. The same results can be obtained according to quasi-operando X-ray photoelectron spectroscopy (XPS). From Figure 5c, 5f and 5i, when the applied potentials increased, the ratio of Fe^{3+}/Fe^{2+} showed a downward trend, the relative content of Fe^{2+} was increased during HER process, and Ni has a similar result (Figure S15-17 and Table S5-6). While the SEM-EDS tests also indicated the surface S content gradually increases with the progress of the electrocatalytic test (Figure S18). Thus, the results clearly inferred the reduction process that occurs on the surface of the material in the HER process.

Conclusion

In this work, we have successfully developed the S-doped $NiFe_2O_4$ nanocrystal (S-$NiFe_2O_4$) by a facile method. The couplings between S doping and oxygen vacancies promote the formation of H_{ads} and performs superior HER activity in the alkaline solution. This catalyst has shown an ultra-low overpotentials and good stability for over 60h at various large current densities. DFT calculations not only reveals the local coordination evolution of Fe sites induced by the S introduction but also confirms the corresponding electronic structure with improved electron transfer capability. The unique structure of S coupling with V_o and optimal electronic environment are the key reason for the low energy barrier of rate determining step, leading to the high efficiency of HER in the alkaline media. Therefore, this works supplies a promising way to optimize the intrinsic activity of metal oxides by the non-metal doping strategy, which offers a novel path to enable industrial-scale H_2 production in the future.

Acknowledgements ((optional))

We acknowledge support from the National Natural Science Foundation of China (NO. 21931001 and 21922105). Special Fund Project of Guiding Scientific and Technological Innovation Development of Gansu Province (2019ZX-04) and the 111 Project (B20027). Bolong Huang acknowledges the support of the Natural Science Foundation of China (NSFC) (No. 21771156), and the Early Career Scheme (ECS) fund (Grant No. PolyU 253026/16P) from the Research Grant Council (RGC) in Hong Kong.

Keywords: keyword 1 • keyword 2 • keyword 3 • keyword 4 • keyword 5

[1] Z. W. Seh, J. Kibsgaard, C. F. Dickens, I. Chorkendorff, J. K. Nørskov,T. F. Jaramillo, Science 2017, 355, eaad4998.
[2] C. Hu, L. Zhang, J. Gong, Energy Environ. Sci. 2019, 12, 2620‐2645.
[3] J. Kim, H. Kim, W.-J. Lee, B. Ruqia, H. Baik, H.-S. Oh, S.-M. Paek, H.-K. Lim*, C. Hyuck. Choi, and S.-I. Choi, J. Am. Chem. Soc. 2019, 141, 45, 18256‐18263.
[4] Y. Zheng, Y. Jiao, A. Vasileff, S.-Z. Qiao, Angew. Chem. Int. Ed. 2018, 57, 7568‐7579.
[5] W. Sheng, H. A. Gasteiger, Y. Shao-Horn, J. Electrochem. Soc. 2010, 157, B1529‐B1536.
[6] J. Joo, T. Kim, J. Lee, S.-I. Choi, K. Lee, Adv. Mater. 2019, 31, 1806682.
[7] J. Yin, J.Jin, H. Lin, Z. Yin, J. Li, M. Lu, L. Guo, P. Xi, Y. Tang, and C.-H. Yan, Adv. Sci. 2020, 7, 1903070
[8] M. A. Khan, H. Zhao, W. Zou, Z. Chen, W. Cao, J. Fang, J. Xu, L. Zhang, J. Zhang, Electrochem. Energy Rev. 2018, 1, 483‐530.
[9] J. Lu, S. Yin, P. Shen, Electrochem. Energy Rev. 2019, 2, 105‐127

[10] K. Zeng, D. Zhang, Prog. Energy Combust. Sci. 2010, 36, 307–326.
[11] S. Xiao, C. Zhou, X. Ye, Z. Lian, N. Zhang, J. Yang, W. Chen, H. Li, ACS Applied Materials & Interfaces 2020, 12, 32604-32614.
[12] J. Greeley, T. F. Jaramillo, J. Bonde, I. B. Chorkendorff, J. K. Norskov, Nat. Mater. 2006, 5, 909-914.
[13] J. K. Norskov, C. H. Christensen, Science 2006, 312, 1322-1323.
[14] T. R. Cook, D. K. Dogutan, S. Y. Reece, Y. Surendranath, T. S. Teets, D. G. Nocera, Chem. Rev. 2010, 110, 6474-6502.
[15] M. G. Walter, E. L. Warren, J. R. McKone, S. W. Boettcher, Q. X. Mi, E. A. Santori, N. S. Lewis, Chem. Rev. 2010, 110, 6446-6473.
[16] Y. P. Zhu, C. Guo, Y. Zheng, S.-Z. Qiao, Acc. Chem. Res. 2017, 50, 915-923.
[17] K. Zeng, D. Zhang, Prog. Energy Combust. Sci. 2010, 36, 307‐326.
[18] N. Mahmood, Y. Yao, J. W. Zhang, L. Pan, X. Zhang, J.J. Zou, Adv. Sci. 2018, 5, 1700464.
[19] Y. Jiao, Y. Zheng, M. Jaroniec, S. Z. Qiao, Chem. Soc. Rev. 2015, 44, 2060-2086.
[20] Y. Zhao, T. Ling, S. Chen, B. Jin, A. Vasileff, Y. Jiao, L. Song, J. Luo, S.-Z. Qiao*, Angew. Chem. Int. Ed. 2019, 131, 12380‐12385.
[21] J. Yin, J. Jin, H. Zhang, M. Lu, Y. Peng, B. Huang, P. Xi, C.-H. Yan, Angew. Chem. Int. Ed. 2019, 58, 18676-18682.
[22] Y. Wu, F. Li, W. Chen, Q. Xiang, Y. Ma, H. Zhu, P. Tao, C. Song, W. Shang, T. Deng, J. Wu, Adv. Mater. 2018, 30, 1803151.
[23] Y. Wu, F. Li, W. Chen, Q. Xiang, Y. Ma, H. Zhu, P. Tao, C. Song, W. Shang, T. Deng, J. Wu, Adv. Mater. 2018, 30, 1803151.
[24] J. Yin, Y. Li, F. Lv, M. Lu, K. Sun, W. Wang, L. Wang, F. Cheng, Y. Li, P. Xi, S. Guo, Adv. Mater. 2017, 29, 1704681.
[25] a) A. Le Goff, V. Artero, B. Jousselme, P. Dinh Tran, N. Guillet, R. Métayé, A. Fihri, S. Palacin, M. Fontecave, Science 2009, 326, 1384-1387; b) T. F. Jaramillo, K. P. Jørgensen, J. Bonde, J. H. Nielsen, S. Horch, I. Chorkendorff, Science 2007, 317, 100-102; c) J. Kibsgaard, Z. Chen, B. N. Reinecke, T. F. Jaramillo, Nat. Chem. 2012, 11, 963-969; d) E. J. Popczun, J. R. McKone, C. G. Read, A. J. Biacchi, A. M. Wiltrout, N. S. Lewis, R, E. Schaak, J. Am. Chem. Soc. 2013, 135, 9267-9270.
[26] a) C. Lei, Y. Wang, Y. Hou, P. Liu, J. Yang, T. Zhang, X. Zhuang, M. Chen, B. Yang, L. Lei, C. Yuan, M. Qiu, X. Feng, Energy Environ. Sci. 2019, 12, 149-156; b) H.-W. Liang, S. Brüller, R. H. Dong, J. Zhang, X. L. Feng, K. Müllen, Nat. Commun. 2015, 6, 7992; c) Y.-R. Zheng, P. Wu, M.-R. Gao, X.-L. Zhang, F.-Y. Gao, H.-X. Ju, R. Wu, Q. Gao, R. You, W.-X. Huang, S.-J. Liu, S.-W. Hu, J. Zhu, Z. Li, S.-H. Yu, Nat. Commun. 2018, 9, 2533; d) L. Cao, Q. Luo, W. Liu, Y. Lin, X. Liu, Y. Cao, W. Zhang, Y. Wu, J. Yang, T. Yao, S. Wei, Nat. Catal. 2019, 2, 134-141.
[27] F.-C. Shen, Y. Wang, Y.-J. Tang, S.-L. Li, Y.-R. Wang, L. Z. Dong, Y.-F. Li, Y. Xu, Y.-Q. Lan, ACS Energy Lett. 2017, 2, 1327–1333.
[28] J. Yin, J. Jin, M. Lu, B. Huang, H. Zhang, Y. Peng, P. Xi, C.-H. Yan, J. Am. Chem. Soc. 2020, 142, 18378‐18386
[29] J. Bao, X. Zhang, B. Fan, J. Zhang, M. Zhou, W. Yang, X. Hu, H. Wang, B. Pan, Y. Xie, Angew. Chem., Int. Ed. 2015, 54, 7399–7404.
[30] J. Gao, C.-Q. Xu, S.-F. Hung, W. Liu, W. Cai, Z. Zeng, C. Jia, H. M. Chen, H. Xiao, J. Li, Y. Huang, B. Liu, J. Am. Chem. Soc. 2019, 141, 3014–3023.
[31] L. Zhuang, L. Ge, Y. Yang, M. Li, Y. Jia, X. Yao, Z. Zhu, Adv. Mater. 2017, 29,1606793.
[32] X. Liang, L. Shi, R. Cao, G. Wan, W. Yan, H. Chen, Y. Liu, X. Zou, Adv. Mater. 2020, 32, 2001430.
[33] a) T. Wu, S. Sun, J. Song, S. Xi, Y. Du, B. Chen, W. A. Sasangka, H. Liao, C. L. Gan, G. G. Scherer, L. Zeng, H. Wang, H. Li, A. Grimaud, Z. J. Xu, Nat. Catal. 2019, 2, 763‐772; b) Y. Zhou, S. Sun, J. Song, S. Xi, B. Chen, Y. Du, A. C. Fisher, F.Cheng, X. W. Wang, H. Zhang, Z. J. Xu, Adv. Mater. 2018, 30, 1802912; c) Y. Zhou, S. Sun, S. Xi, Y. Duan, T. Sritharan, Y. Du, Z. J. Xu, Adv. Mater. 2018, 30, 1705407.
[34] J.-X. Feng, J.-Q. Wu, Y.-X. Tong, G.-R. Li, J. Am. Chem. Soc. 2018, 140, 610‐617.
[35] H. Liu, Q. He, H. Jiang, Y. Lin, Y. Zhang, M. Habib, S. Chen, L. Song, ACS Nano 2017, 11, 11574‐11583.
[36] R. Miao, B. Dutta, S. Sahoo, J. He, W. Zhong, S. A. Cetegen, T. Jiang, S. P. Alpay, S. L. Suib, J. Am. Chem. Soc. 2017, 139, 13604‐13607.
[37] J. Liu, Y. Liu, N. Liu, Y. Han, X. Zhang, H. Huang, Y. Lifshitz,* S.-T. Lee, J. Zhong, Z. Kang, Science. 2015, 347. 970-974.

.

Layout 1:

RESEARCH ARTICLE

Text for Table of Contents

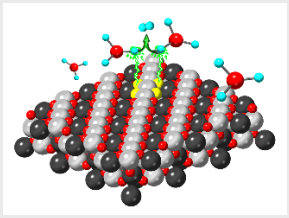

*Author(s), Corresponding Author(s)**

Page No. – Page No.

Title